World Scientific
www.worldscientific.com

Diagnosis of knee osteoarthritis by OCT and surface-enhanced Raman spectroscopy

Ran An*, Huaimin Gu*,‖, Zhouyi Guo†, Huiqing Zhong†, Huajiang Wei†,
Guoyong Wu‡, Yonghong He§, Shusen Xie¶ and Hongqin Yang¶

*School of Semiconductor Science and Technology
South China Normal University, Guangzhou 510631, P. R. China

†Publications Department, Optica
2010 Massachusetts Avenue NW, Washington, DC 20036
MOE Key Laboratory of Laser Life Science &
Institute of Laser Life Science, College of Biophotonics
South China Normal University
Guangzhou 510631, P. R. China

‡The First Affiliated Hospital of Sun Yat-Sen University
Guangzhou 510080, P. R. China

§Tsinghua University, Shenzhen 518055, P. R. China

¶Fujian Normal University
Key Laboratory of Optoelectronic Science and
Technology for Medicine of Ministry of Education of China
Fuzhou 350007, P. R. China
‖guhm139@139.com

In this paper, optical coherence tomography (OCT) and surface-enhanced Raman spectroscopy (SERS) were used to characterize normal knee joint (NKJ) tissue and knee osteoarthritis (KOA) tissue *ex vivo*. OCT images show that there is a clear hierarchical structure in NKJ tissue, including surface layer, transitional layer, radiation layer and cartilage matrix calcification layer tissue structure, while the hierarchical structure of KOA tissue is not clear and unevenly distributed, and the pathological tissues at different stages also show significant differences. SERS shows that NKJ tissue and mild osteoarthritic knee cartilage (MiKOA) tissue have strong characteristic Raman peaks at 964, 1073 (1086), 1271, 1305, 1442, 1660 and 1763 cm^{-1}. Compared with the Raman spectrum of NKJ tissue, the Raman characteristic peaks of MiKOA tissue have some shifts, moving from 1073 cm^{-1} to 1086 cm^{-1} and from 1542 cm^{-1} to 1442 cm^{-1}. There is a characteristic Raman peak of 1271 cm^{-1} in MiKOA tissue, but not in NKJ tissue. Compared

‖Corresponding author.

with NKJ tissue, severely degenerated cartilage (SdKOA) tissues show some new SERS peaks at 1008, 1245, 1285, 1311 and 1321 cm^{-1}, which are not seen in SERS spectra of NKJ tissue. Principal component analysis (PCA) was used to analyze the Raman spectra of 1245–1345 cm^{-1} region. The results show that PCA can distinguish NKJ, MiKOA and SdKOA tissues and the accuracy is about 90%. These results indicate that OCT can clearly distinguish NKJ, MiKOA, moderate osteoarthritic knee cartilage (MoKOA) and SdKOA tissue, while SERS can provide further judgment basis. The results also prove that the contents of protein and polysaccharide in knee tissue are changed during the pathological process of knee tissue, which is the cause of pain caused by poor friction in knee joint during movement.

1. Introduction

Osteoarthritis (OA) is a joint degenerative disease that seriously affects the quality of life of patients, causing huge economic burden to patients, families and society.[1,2] Knee osteoarthritis (KOA) is the most common form of arthritis in the world, and its incidence rate increases with age. With the aging population, the number of cases increases every year. About 250 million people worldwide suffer from knee arthritis, including 9.6% of men and 18% of women after the age of 60.[3] According to the survey, the prevalence rate of KOA in the elderly over 65 years old in the United States is 33.6%, and the prevalence rate in women (42.1%) is higher than that in men (31.2%).[4] In addition to aging, the incidence of KOA caused by trauma and obesity is also gradually increasing in the young population.[5] KOA is a complex disease involving the entire synovial joint including articular cartilage, synovial membrane and subchondral bone.[6,7] The loss of articular cartilage has been thought to be the major change, but the combination of cellular changes and biomechanical stress leads to a number of secondary changes, including subchondral bone remodeling, osteophyte formation, development of bone marrow lesions, changes in synovium, joint capsule, ligaments and periarticular muscles, meniscus tearing and squeezing.[8–11] Early KOA is mainly manifested as intermittent pain, mainly joint space pain, aggravated after activity and relieved after rest. Pain is usually associated with changes in the weather, and cold and humidity can aggravate the pain. As the disease progresses, there may be resting pain or even nocturnal pain.[12]

For patients with early knee arthritis, weight loss and diet regulation can alleviate knee pain and restore function.[13] Drugs can quickly alleviate the pain and functional limitations of knee arthritis, but they may also have toxic effects on systemic organs. Studies have shown that arthroscopic patellofemoral decompression is effective in the treatment of patellofemoral degeneration. It can alleviate pain and improve knee function, which is worthy of clinical application.[14] However, this method is only applicable to patients with early knee osteoarthritis, and has no obvious effect on patients with knee arthritis. At present, some clinical methods, such as MRI and CT, also have some deficiencies in some aspects. For example, MRI radiation may bring some negative effects to the human body. Therefore, early detection of knee joint lesions is very important. However, there is still a lack of effective technology to detect early knee lesions at the molecular level. In recent years, infrared spectroscopy,[15] near infrared spectroscopy,[16] fluorescence spectroscopy[17] have been applied to study the biochemical components of articular cartilage, while these spectral techniques have corresponding defects in detecting knee joint. Raman spectroscopy[18] can noninvasively analyze cartilage tissue and is not affected by water in tissue.[19] However, the conventional Raman spectroscopy signal is very weak, easy to be disturbed by fluorescence signal, and the detection sensitivity is low. Surface enhanced Raman spectroscopy can significantly improve the signal intensity of Raman spectrum and eliminate fluorescence interference. It has the advantages of fast, high sensitivity, less sample consumption and simple sample preparation. It has become a promising biomedical detection method.

Optical coherence tomography (OCT) is a non-invasive technique based on low-coherence interferometry, which is very sensitive to changes in the optical properties of biological tissues.[20,21] OCT imaging can provide more information about the properties of cartilage tissue than independent

arthroscopy. By measuring the light intensity on and below the cartilage surface, high-resolution cross-sectional images can be captured in real time. It can provide 10–100 times higher resolution than current clinical imaging technology.[22] Previous studies have shown a high correlation between OCT images and reference histology.[23–25] So far, the *in vivo* applicability of OCT has been demonstrated in open knee surgery[22] and arthroscopy.[26] Further studies show that OCT may detect early cartilage degeneration caused by meniscus injury[27] or mechanical injury.[28]

In this paper, the imaging and spectral studies of normal knee joint (NKJ), mild osteoarthritic knee cartilage (MiKOA), moderate osteoarthritic knee cartilage (MoKOA) and severely degenerated cartilage (SdKOA) tissues were carried out by combination of OCT and SERS technology. Usually, OCT can realize imaging based on the backscattering of normal tissue and diseased tissue to light, and recognize and distinguish different tissues from the aspect of histomorphology based on the differences of the images, while surface-enhanced Raman spectroscopy (SERS) can recognize and distinguish different tissues from the aspect of tissue composition based on the differences of SERS spectra and Raman peaks between normal tissue and arthritis tissue, As a supplementary method, SERS can provide further recognition basis for distinguishing normal tissues from diseased tissues. Therefore, we hope that through the research work of this paper, the feasibility of using OCT/SERS method to identify and distinguish normal bone tissue and diseased bone tissue can be explored, so OCT/SERS method can be used in the diagnosis of bone lesions. It is hoped that with the development of OCT and SERS technology and the deepening of research work, OCT/SERS can become one of the methods that can be selected for relevant clinical applications in the future.

2. Materials and Methods

2.1. *Instrumentation*

The OCT system used in this experiment is a portable Fourier domain OCT system controlled automatically by computer. Its central wavelength is 840 nm, the bandwidth is 80 nm, and the lateral and in-depth resolutions are 30 μm and 7.8 μm, respectively. The transverse and depth scanning ranges are 3 mm and 1.8 mm, respectively. The B-scans

obtained in each experiment are stored in the computer for further processing. The data acquisition software is written with Lab VIEW 7. A schematic diagram of the OCT system can be found in the literature.[29,30]

SERS measurement and data preprocessing: In this experiment, the Raman spectra of the samples were collected by a confocal Raman microscopy (Renishaw, in Via, United Kingdom), which collects spectra from backscattering geometry by a Leica DM-2500 microscope equipped with objective 20×. The excitation light source is 785 nm diode laser. The power of laser irradiation is about 1 mW and the spot diameter is about 5 μm. The spectral acquisition range is 800–1860 cm^{-1}. The spectral resolution is about 1 cm^{-1} (It is from the technical parameters of the instrument used in experiment) and the spectrograph grating used is a 1200 g/mm grating. Each Raman spectrum was collected six times, and the integration time of each time was 10 s. Before collecting the Raman spectrum of the experimental sample, the instrument was calibrated by using the Raman spectrum of silicon in 520 cm^{-1} band. The software package WIRE 3.2 (Renishaw) was used for spectrum acquisition and analysis. All data were acquired under the same conditions.

2.2. *Tissue preparation and experimental procedure*

Tissue Preparation: Knee-joint tissue samples were collected from 24 patients (aged between 68 and 78) undergoing knee replacement surgery, and 2–3 samples can be selected from each patient's surgical tissue for OCT or Raman experiment. All patients were from the Department of Orthopedic Surgery, the First Affiliated Hospital of Sun Yat-sen University. The tissues (a part of the knee) collected from the hospital were divided into approximately 2×2 cm^2, and the thickness is about 0.5 cm. The samples were washed with saline, the blood on surface was removed. Then, these samples were placed in different plastic boxes and kept in an ultra-low temperature refrigerator at $-80°$C as soon as possible. These samples were divided into NKJ and KOA groups. The NKJ group and the KOA group were divided into control group (The samples of control group is only used for the relevant experiments to verify the enhancement effect of nanoparticles in Fig. 7) and experimental group (Other samples except the control group).

Experimental procedure: Before each experiment, the samples taken from the low-temperature refrigerator were placed at room temperature for 30 min. Then, only normal saline was added to the samples of the control group, while normal saline and silver nanoparticles (Ag NPs) solution were added to the samples of the experimental group at the same time. The nanoparticle concentration of the solution used in the experiment is 0.1 mol/L. Since the time of obtaining Raman image is much shorter than that of OCT, the samples were first used to measure the Raman data, and then used for obtaining the OCT image. During data measurement, the sample is placed in a petri dish with normal saline. Because the penetration of nanoparticles in cartilage changes with time, in order to obtain the change law of OCT image with time, we explore the change of OCT signal slope of cartilage tissue with time in the process of nanoparticle penetration, and improve the reliability of experimental data, we conducted 4 h continuous OCT imaging for each sample, recorded an OCT image every minute. Then the clearest OCT image was selected for relevant data analysis.

SERS measurement: The sample taken from the low-temperature refrigerator was placed at room temperature for 30 min. The sample of experimental group was added with 2 ml Ag NPs solution, and 2 ml Ag NPs solution was added again 10 min later. The sample of control group was added with 2 ml normal saline, and 2 ml normal saline was added again 10 min later. 5 min later, the Raman spectrum of the sample was measured by SERS system. SERS spectra data were collected five times for each sample and averaged. The data collected were smoothed, and baseline correction and noise removal were also performed.

OCT data acquisition: The OCT system was used to collect OCT image for each prepared sample, once every 1 min, and continuously monitor for 4 h for each sample. A total of 240 OCT images were obtained for each experimental sample.

2.3. Synthesis of Ag NPs

The preparations of Ag NPs are as follows. Before the experiment, the tetrafluoroethylene magnets and the glass instruments related to the experiment were put into an acidic solution for eight hours, then, they were rinsed with deionized water, and dried in an oven for experimental use. Ag NPs solution was prepared by reducing $AgNO_3$ solution with sodium citrate.[31] First, 18 mg $AgNO_3$ (99.8%, Shanghai, China) was dissolved in a beaker and was put into a 100 ml volumetric flask. Second, the $AgNO_3$ solution was poured into the flask and heated to boiling while stirring; at this time, 2 ml of 1% sodium citrate aqueous solution was quickly added to the solution. Finally, the above mixture was kept slightly boiling under stirring for about 60 min, until the solution turned celadon, and then the heating was stopped. The mixture was cooled to room temperature with stirring. The resulting solution is stored at $-4°C$ for experiment.

Ag NPs were characterized by scanning electron microscope (SEM) (FEG Quanta 250, America) and ultraviolet visible (UV-2600, Japan) spectroscopy. Samples for SEM were prepared by dropping the particle suspensions onto a silicon slice and evaporating. The electron micrographs of Ag NPs are shown in Fig. 1(a). Ag NPs are uniform in shape and size. The average particle size can be determined by counting (Nano Measurer 1.2) more than 200 particles. The size of Ag NPs is mostly between
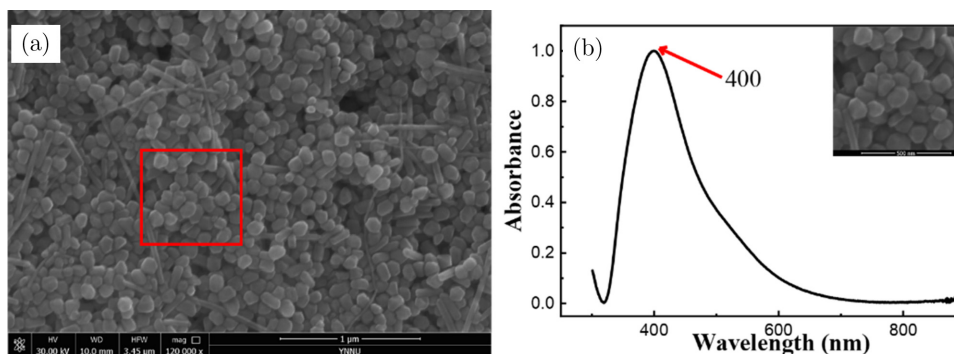

Fig. 1. SEM images and UV-Vis spectra of Ag NPs. (a) SEM of Ag NPs and (b) UV-Vis spectra of Ag NPs.

60 nm and 70 nm. It can be seen from the figure that silver nanorods exist in the solution, while relevant studies have proved that silver nanorods also have good surface enhancement.[32] The illustration in Fig. 1(b) is an enlarged view of part of Fig. 1(a). Figure 1(b) shows the UV-visible near infrared absorption spectrum of Ag NPs. The UV-Vis absorption peak of Ag NPs appears at 400 nm.

2.4.   *Data analysis*

2.4.1.   *OCT data analysis*

In this study, cartilage tissues (including NKJ tissues and OA tissues) were continuously examined by OCT. An average of A-scans was taken from a horizontal surface of each OCT B-scan. B-scans images obtained from each test were stored in a computer for further processing. Through ImageJ data processing software, the signal strength at a specific depth of the OCT image of the sample was first integrated along the x-axis within the box area (as shown in Fig. 2(a)), and the average processing was done. Then, the OCT signal strength of the

corresponding depth was obtained. Through data processing of image at other depth by similar methods, the one-dimensional distribution of OCT signal strength within the whole imaging depth range with depth can be achieved. By integrating the signal strength of the whole area of OCT image at a certain time point of a sample, the total OCT signal strength of the sample at the corresponding time was obtained. Similar data processing was performed on 240 OCT images obtained within 4 h to obtain the distribution of the OCT signal strength of the sample with time. Then, the change of OCT signal slope with time can be obtained by data processing software. The linear region with the minimum fluctuation of 1D OCT signal was selected to analyze the changes of optical properties of the samples over time.

OCT imaging is based on the difference of light attenuation. The change of OCT signal with depth follows Lambert–Beer law.[33] According to Lambert–Beer law, the light attenuation law in tissue is exponential. The average signal intensity data of cartilage tissue in NKJ group and OA group
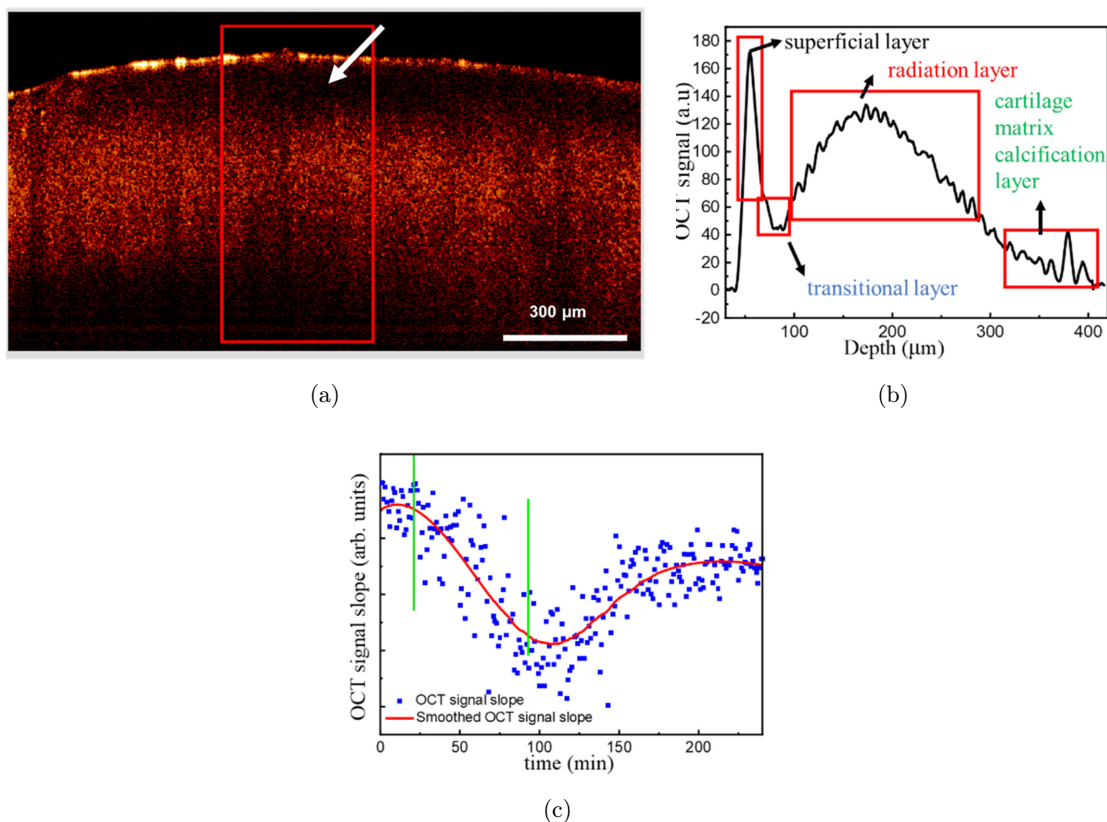

(a)

(b)

(c)

Fig. 2.   B-scans and corresponding one-dimensional OCT signal images of NKJ tissue. (a) OCT image; (b) OCT signal; (c) OCTSS graph of NKJ: The two vertical lines area represents the Ag NPs diffusion interval.

were obtained by exponential fitting curve. The fitting equation is applicable to OCT signals in cartilage tissue:

$$y = A \exp(\mu x) + y_0, \qquad (1)$$

where μ is the attenuation coefficient and x is the penetration depth.

2.4.2. *SERS data analysis*

When the monochromatic light beam with frequency v_0 irradiates on the material, some of them are transmitted, some are reflected and some are scattered. In the scattered light, in addition to the light with the same frequency as the incident light v_0, there is also a series of light with the frequency of $v_0 \pm \Delta v_i$. The light whose frequency changes is Raman scattering light, where Δv_i is the Raman shift.[34,35]

In order to confirm that SERS spectroscopy data can indeed play a role in distinguishing and identifying normal tissues and diseased tissues, PCA analysis on the SERS data obtained from the experiment was performed.

PCA aims to model the variance–covariance structure of a data matrix and extract the eigenvalues corresponding to the principal components.[36] Each principal component is a linear combination of the n independent wavenumber variables x_1, x_2, x_3, ..., x_n. For example:

$$PC_1 = a_1 x_1 + a_2 x_2 + a_3 x_3 + \cdots + a_n x_n. \qquad (2)$$

In this paper, we first calibrate the baseline, remove the background and normalize the SERS spectroscopy data through Origin software. Then, the SERS spectroscopy data in the range of 925–1025 cm^{-1} and 1245–1345 cm^{-1} of 27 samples including nine NKJ tissues, nine MiKOA tissues and nine SdKOA tissues were extracted, respectively, Then, PCA analysis based on SERS spectroscopy data in the range of 925–1025 cm^{-1} and 1245–1345 cm^{-1} was carried out by using Unscrambler $\times$ 10.4 (Camo software as, Oslo, Norway) software, so as to confirm the role of SERS spectroscopy in distinguishing and identifying normal tissues and diseased tissues.

3. Results and Discussion

3.1. *OCT image analysis*

Figure 2(a) is the OCT image of NKJ tissue, and Fig. 2(b) is the corresponding OCT intensity profile. As shown in Fig. 2(a), the layered structure of NKJ tissue (superficial layer, transitional layer, radiation layer and cartilage matrix calcification layer) is clearly visible. It indicates that the normal cartilage layer is arranged in dense and orderly order. OCT images of NKJ tissue show smooth and uniform surface of cartilage (Fig. 2(a)). OCT signals are strongest in the surface layer of cartilage, and then decreases significantly in the transition layer below the surface layer (white arrow). In the radiation layer, the signal becomes stronger again, and maintains a strong signal in a wide area, and then gradually weakens. At the bottom is the calcification layer, where there is a strong signal. These correspond to the one-dimensional signals of OCT.

Figure 2(c) shows a typical OCTSS diagram during the penetration of Ag NPs into cartilage tissue. It can be found that after adding the Ag NPs solution, the penetration of Ag NPs in the tissue causes the change of optical properties of the tissue. The OCT signal begins to enhance and the OCTSS rises slowly. After about 25 min, the OCT signal enhancement speed slows down and the signal slope begins to decline. With the further penetration of Ag NPs, the OCT signal tends to be saturated. After that, due to the infiltration of water on the surface of the tissue into the tissue, the relative concentration of Ag NPs in the tissue decreases, the OCT signal begins to decline, and the OCTSS further decreases. At about 100 min, the decline speed of OCT signal slows down and the OCTSS reaches the minimum value and then it begins to rise again. At about 180 min, the OCTSS reaches the equilibrium. It is worth noting that although the scattering of nanoparticles may cause the signal-to-noise ratio of OCT image to change, such as affecting the baseline of OCT data, in terms of comparing the penetration difference of nanoparticles in the different tissue and the relative distribution of nanoparticles in the tissue, and realizing the qualitative discrimination and identification of the tissue, the scattering of nanoparticles should not affect the final analysis conclusion. This is because the penetration and distribution of nanoparticles in the tissue are initially affected by the tissue difference.

Figure 3 shows a representative OCT image of early knee cartilage injury (Fig. 3(a)) and the corresponding OCT intensity distribution (Fig. 3(b)). Comparing Figs. 2 and 3, it can be found that, similar to NKJ tissues, the OCT signal on the surface layer of MiKOA tissue is the strongest, and the OCT signal on the radiation layer becomes weaker.
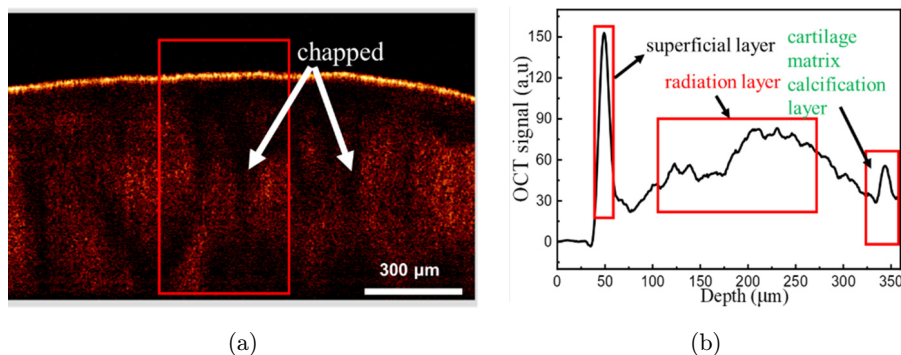
(a)   (b)

Fig. 3. Two-dimensional OCT image and corresponding one-dimensional OCT signal images of MiKOA tissue. (a) OCT image and (b) OCT signal.

OCT images show that the cartilage surface of MiKOA tissue is similar to that of NKJ tissue, which is relatively complete, but the bone tissue of the radiation layer of MiKOA tissue is unevenly distributed and cracked.

Figure 4 shows a representative OCT image of MoKOA tissue (Fig. 4(a)) and the corresponding OCT signal intensity distribution (Fig. 4(b)). Regions of diminished back scattering can be observed in the OCT image, which is associated with areas of hypocellularity and diminished matrix in histological preparations.[22] OCT images show that the cartilaginous layer is significantly thinner and separated from the calcified layer. In addition, subchondral bone tissue is disordered. As can be seen from Fig. 4(b), the OCT signal strength of the cartilage layer is weakened, while the OCT signal strength of the calcified layer is strongest.

Figure 5 shows the OCT image of severe knee joint lesions cartilage (Fig. 5(a)) and the corresponding OCT signal intensity distribution (Fig. 5(b)). As can be seen from Fig. 5(a), the surface layer of cartilage is extremely uneven. It is difficult to identify the interface between the surface layer of

cartilage and the transitional layer. In the middle part of the OCT image, cartilage is missing and bone is exposed to the surface.[22] As can be seen from Fig. 5(b), the OCT signal intensity of the cartilage layer decreases or even disappears, while the OCT signal intensity of the calcified layer is the strongest. Figure 5(c) is a picture of SdKOA tissue. It can be observed that the cartilage surface layer (white arrow) loses its initial function and the cartilage even disappears. The inset is a back view of the knee joint. Figure 5(d) shows the OCT image changes of SdKOA tissue within 4 h before and after the application of Ag NPs. Due to the penetration and accumulation of Ag NPs in the tissue, the overall OCT image becomes brighter and clearer with the passage of time. The main reason is the strong backscattering of probe light by Ag NP, which indicates that more Ag NP diffuses into cartilage tissue. After 3 h, the intensity of OCT signals almost no longer changes, indicating that the infiltration and accumulation of Ag NP in knee cartilage reach a balance.

In order to visually compare the differences between NKJ, MiKOA, MoKOA and SdKOA tissues,
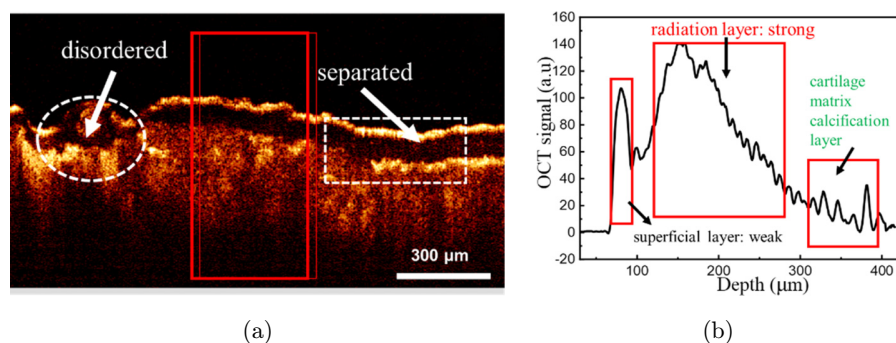

(a)   (b)

Fig. 4. Two-dimensional OCT image and corresponding one-dimensional OCT signal images of MoKOA tissue. (a) OCT image and (b) OCT signal.
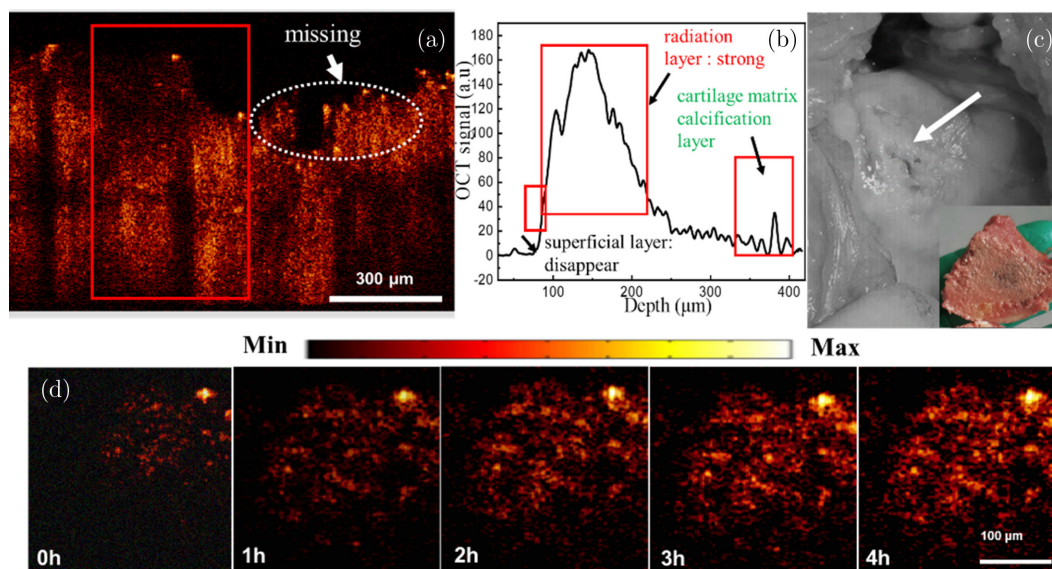
Fig. 5. B-scans, corresponding one-dimensional OCT signal images and Surgical image of SdKOA tissue. (a) OCT image, (b) OCT signal, (c) Surgical image and (d) OCT images of SdKOA tissue during 4 h of application of Ag NPs.
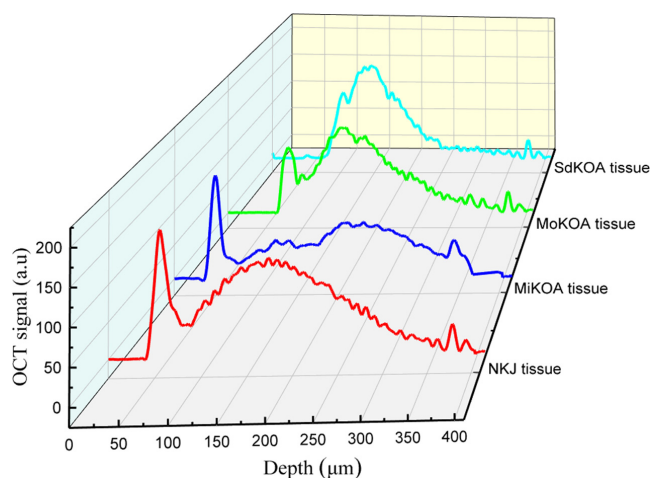

Fig. 6. One-dimensional OCT images of NKJ, MiKOA, MoKOA and SdKOA tissues.

The 1D OCT signal diagrams of NKJ, MiKOA, MoKOA and SdKOA tissues are shown together in Fig. 6. It can be found that the distribution of one-dimensional OCT signal intensity in depth direction is quite different in different tissues. Compared with NKJ tissue, the OCT signal intensity of the radiation layer of MiKOA tissue decreases, and the OCT signal intensity of the surface layer tissue does not change significantly, while the OCT signal intensities of the radiation layer of MoKOA and SdKOA tissue increase significantly. Moreover, from the distribution of OCT signal intensity, there is no obvious distinction between the surface layer and

radiation layer of MoKOA and SdKOA tissue. Pathologically, the typical pathological changes after knee lesions mainly occur in the articular cartilage layer. The knee cartilage will degenerate and degenerate, and the subchondral bone will harden or calcify. The change of the tissue structure of the surface layer of MiKOA tissue leads to the change of its optical properties, which reduces the OCT signal intensity of the radiation layer below it. With the further development of knee arthritis, chondrocytes further degenerate and apoptosis. The cartilage surface layer of MoKOA and SdKOA tissue is incomplete or even disappeared, and the radiation layer tissue is exposed. These changes in tissue structure leads to the increase of OCT signal intensity in the radiation layer of MoKOA and SdKOA tissues, and the boundary between the surface layer and the radiation layer disappears. This shows that with the progress of knee arthritis, the morphological structure of its tissue has indeed undergone some changes. With the aggravation of the disease, the difference between its tissue structure and normal tissue is becoming larger and larger, which leads to a great difference in the distribution of OCT signal intensity with depth.

3.2. Raman spectrum analysis

In order to study the changes in the composition and deep microstructure of knee cartilage and sub
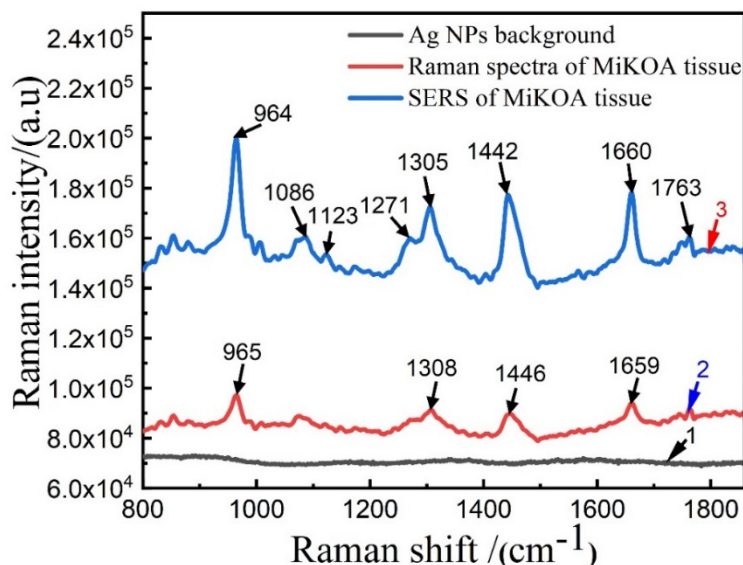
Fig. 7. Raman spectra of MiKOA tissue. Raman spectra of Ag NPs background, Raman spectra of MiKOA tissue and SERS spectra of MiKOA tissue.

bone tissue during the progression of the lesion, Raman spectroscopy was used to study NKJ, MiKOA and SdKOA tissues. In order to verify that the nanoparticle solution used in the experiment as the Raman enhancement matrix has a strong enhancement effect on the SERS spectroscopy signals of the sample, The conventional Raman spectroscopy (Samples was from the control group) and SERS technology (Samples of the experimental group were used) were used to study the MiKOA tissue for comparative analysis. Figure 7 shows the conventional Raman spectrum and SERS spectrum of MiKOA tissue in the range of 800–1860 cm^{-1} (The number of samples used to obtain each spectrum is about 9, and the best spectrum is selected as the experimental data). The results show that the conventional Raman spectroscopy signal is relatively weak, only weak Raman characteristic peaks were detected at 965, 1308, 1446 and 1653 cm^{-1}. Compared with the conventional Raman spectrum, the SERS spectrum of MiKOA tissue is significantly enhanced, and the overall Raman signal intensity is significantly improved. At the same time, in addition to the above conventional Raman characteristic peaks, new Raman characteristic peaks were detected at 1086 cm^{-1} and 1271 cm^{-1}. From Fig. 7, it can be found that the Raman spectrum of MiKOA tissue shows some Raman spectra characteristics of hydroxyapatite phosphate and hydroxyapatite carbon, and the characteristic Raman peak at 964 cm^{-1} is v_1 symmetrical tensile vibration

of v_3 PO$_4^{3-}$ (hydroxyapatite phosphate (PO$_4$). The characteristic Raman peak at 1086 cm^{-1} corresponds to the Tensile vibration of CO of hydroxyapatite carbonate. After surface enhancement, MiKOA tissue shows a Raman peak of glucose at 1123 cm^{-1}. The characteristic peak at 1271 cm^{-1} is the Tensile vibration of C–N and the bending vibration of N–H in amide III band. These results are also consistent with the results of the relevant literature.[37–39] The important vibration peak in this interval is 1660 cm^{-1}, which is the Tensile vibration peak of C = O double bond in amide I band. The peak 1442 cm^{-1} is the antisymmetric vibration peak of CH$_2$/CH$_3$ (phospholipid). There are a series of characteristic vibration peaks at 1442, 1445 and 1305 cm^{-1}. They all belong to the deformation vibration peak of CH$_2$/CH$_3$ in unsaturated fatty acid chain.[40–42] Their existence is produced by methyl and methylene in long-chain fatty acid molecules. The frequency and distribution of Raman features[43–45] are shown in Table 1.

Figure 8 shows the SERS spectra of NKJ, MiKOA and SdKOA tissues. Figure 8(a) shows SERS spectra of NKJ cartilage tissues and MiKOA cartilage tissues in the range of 800–1860 cm^{-1}. As can be seen from Fig. 8(a), the SERS spectroscopy signal of MiKOA tissue is much stronger than that of NKJ tissue. The characteristic peaks of NKJ appear at 964, 1073, 1306, 1452 and 1660 cm^{-1}. Raman peaks of MiKOA tissue are at 964, 1086, 1271, 1305, 1442, 1660 and 1763 cm^{-1}. Compared

Table 1.   Raman frequency and distribution in human knee tissue.

Frequency (cm^{-1})	Assignment (proteins) local coordinate
854	(C–O–C) polysaccharides
961–965	Symmetric stretching vibration of v_1 PO$_4^{3-}$ (phosphate of hydroxyapatite)
1074	Carbonate symmetric stretching vibration of calcium carbonate apatite
1087	v_1 CO$_3^{2-}$, v_3 PO$_4^{3-}$, v(C–C) skeletal of acyl backbonein lipid (gauche conformation)
1123	Glucose
1269	v (CN) and δ (NH) amide III
1308	δ (CH$_2$) deformation (lipid), adenine, cytosine
1448	δ (CH$_2$) and δ (CH$_3$)
1658	Amide I v (C=O) of proteins

Note: v: stretching vibration and δ: bending vibration.

with the SERS spectra of NKJ, the Raman characteristic peaks of MiKOA tissue have some shifts, moving from 1073 cm^{-1} to 1086 cm^{-1} and from 1542 cm^{-1} to 1442 cm^{-1}. At the same time, the MiKOA tissue has a new Raman characteristic peak at 1271 cm^{-1} which does not appear in the SERS spectra of the NKJ tissue. These results show that the contents of protein, lipid and polysaccharide in knee tissue are changed due to the pathological changes of knee joint. Therefore, it is speculated that the changes of these substances are the cause of local redness and pain of knee joint. Figure 8(b) shows SERS spectra of NKJ cartilage tissues and SdKOA cartilage tissues in the range of 800–1860 cm^{-1}. As can be seen from Fig. 8(b), the SERS spectroscopy signal of SdKOA tissue is much stronger than that of NKJ tissue. In the range of 1244–1344 cm^{-1}, the NKJ tissue only shows a Raman peak at 1306 cm^{-1}, while the SdKOA tissue shows more Raman peaks, at 1245, 1256, 1272, 1285, 1297, 1311, 1321 and 1344 cm^{-1}. Compared with the SERS spectra of NKJ, the characteristic peaks of SdKOA tissue move from 964 cm^{-1} to 943 cm^{-1}, from 1452 cm^{-1} to 1453 cm^{-1}, from 1661 cm^{-1} to 1671 cm^{-1} and from 1763 cm^{-1} to
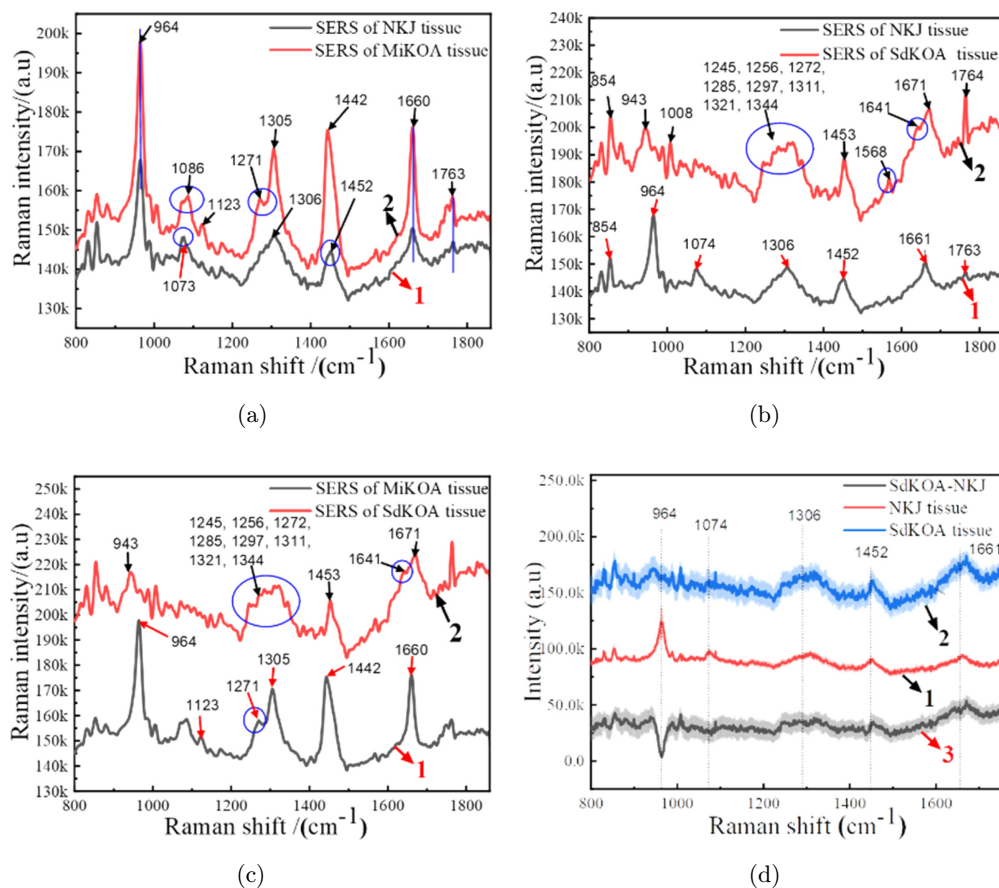

Fig. 8.   SERS spectra of NKJ, MiKOA and SdKOA tissues in the range of 800–1860 cm^{-1}. (a) SERS spectra of NKJ and MiKOA tissues; (b) SERS spectra of NKJ and SdKOA tissues; (c) SERS spectra of MiKOA and SdKOA tissues; (d) SERS spectra of MiKOA, SdKOA tissues and SdKOA-NKJ difference spectrum.

$1764\,\mathrm{cm}^{-1}$. On the other hand, the SdKOA tissue has some new Raman characteristic peak at 854, 1008, 1568 and $1641\,\mathrm{cm}^{-1}$ which don't appear in the SERS spectra of NKJ tissue. While the Raman characteristic peak at $1074\,\mathrm{cm}^{-1}$ of NKJ does not appear in the SERS spectra of the SdKOA tissue. The Raman peak at $854\,\mathrm{cm}^{-1}$ is the vibration of C–O in the polysaccharide, indicating the increase of sugar content in the process of cartilage tissue lesion.

It can be seen from the intensities of the Raman peaks that the overall intensity of SERS spectra of SdKOA tissue is greater than that of MiKOA tissue. Compared with the SERS spectra of the MiKOA tissue, the characteristic peaks of SdKOA tissue move from $964\,\mathrm{cm}^{-1}$ to $943\,\mathrm{cm}^{-1}$, from $1305\,\mathrm{cm}^{-1}$ to $1311\,\mathrm{cm}^{-1}$, from $1442\,\mathrm{cm}^{-1}$ to $1453\,\mathrm{cm}^{-1}$, from $1660\,\mathrm{cm}^{-1}$ to $1671\,\mathrm{cm}^{-1}$ and from $1763\,\mathrm{cm}^{-1}$ to $1764\,\mathrm{cm}^{-1}$. SdKOA tissues have more Raman peaks than MiKOA tissues. The SdKOA tissue has some new Raman characteristic peaks at 1008, 1245, 1272, 1344, 1568 and $1641\,\mathrm{cm}^{-1}$ which don't appear in the SERS spectra of MiKOA tissue. While the Raman characteristic peak at $1086\,\mathrm{cm}^{-1}$ of MiKOA tissue does not appear in the SERS spectra of the SdKOA tissue. These results are also consistent with the results of OCT images. As can be seen from Figs. 2(a) and 3(a), the surface cartilage of NKJ and MiKOA tissue are almost intact, but the layered structure changes significantly. Therefore, compared with the SERS spectra of NKJ tissue, the Raman peak intensities of MiKOA tissue have obvious changes, and its Raman spectra have some frequency shifts or new Raman characteristic peaks. As can be seen from Fig. 5(a), not only the layered structure of SdKOA tissue changes significantly, but also its surface cartilage almost disappears. Therefore, compared with the Raman spectra of NKJ and MiKOA tissue, the Raman characteristic peaks of SdKOA tissue have a more obvious shift, and some new Raman peaks also appear. These results indicate that the content of protein, lipids and polysaccharides in the knee joint tissue have been changed in the course of knee joint disease. In Fig. 8(d), 1 and 2 show the average SERS spectra of NKJ tissue and SdKOA tissue, respectively. In Fig. 8(d), 3 shows the difference between the spectra of SdKOA tissue and NKJ tissue. It can be found that there are some differences in SERS spectra and Raman peak intensities of SdKOA tissue and NKJ tissue. The SERS spectral intensity of SdKOA tissue is generally greater than that of NKJ, but the relative intensity of the Raman peak of NKJ at $964\,\mathrm{cm}^{-1}$ is greater than that of SdKOA tissue. This is also consistent with the research results of relevant literature.[46] The spectra of SdKOA tissue show a decrease in phosphate characteristics, indicating that some changes have taken place in tissue composition. Pathologically, after the occurrence of knee joint lesions, the knee joint cartilage will degenerate and degenerate, and the subchondral bone will harden. The cartilage surface of the SdKOA tissue has seriously degenerated or even disappeared. So the SERS spectra measured in the experiment may include the joint contribution of cartilage tissue and subbone tissue. It is these changes in the structure, morphology and composition of the tissue that leads to the changes in the Raman spectra, Raman peak, the signal-to-noise ratio and signal strength. Our current research results can only qualitatively infer that some changes may have taken place in the composition of the tissue through the Raman spectrum changes of the diseased tissue in different stages, so that we can qualitatively distinguish the normal tissue and the diseased tissue through the Raman spectrum changes in the future practical application. The specific correlation between the characteristic peaks of the Raman spectra and the biochemical or pathological characteristics needs to be further studied.

In order to better distinguish NKJ, MiKOA and SdKOA tissues, principal component analysis was used to analyze SERS spectra data and extract useful information. To evaluate the classification effect of the proteins and lipid-associated range on NKJ, MiKOA and SdKOA tissues, PCA analysis was performed on the SERS spectra in the range of 1245–$1345\,\mathrm{cm}^{-1}$. The correlation containing 27 variables is shown in Fig. 9. It can be seen that the NKJ samples are scattered on the right of the scatter plot, the MiKOA tissue samples are in the middle of the scatter plot, and the SdKOA tissue samples are on the left side of the scatter plot. The contribution rates of PC-1 and PC-2 are 84% and 8%, respectively, and the total contribution rate reaches 92%. The results indicate that PCA based on the SERS spectra in the range of 1245–$1345\,\mathrm{cm}^{-1}$ can better distinguish NKJ, MiKOA and SdKOA tissues.

Then, PCA analysis was also carried out based on the SERS spectra in the range of 925–$1025\,\mathrm{cm}^{-1}$ of NKJ, MiKOA and SdKOA tissue. The characteristic Raman peaks in this range are mainly the SERS spectra of phosphate, protein and
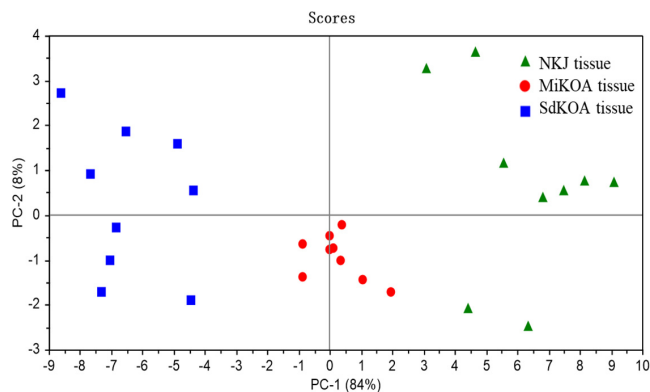
Fig. 9.   Principal component scores plot of NKJ, MiKOA and SdKOA tissues.
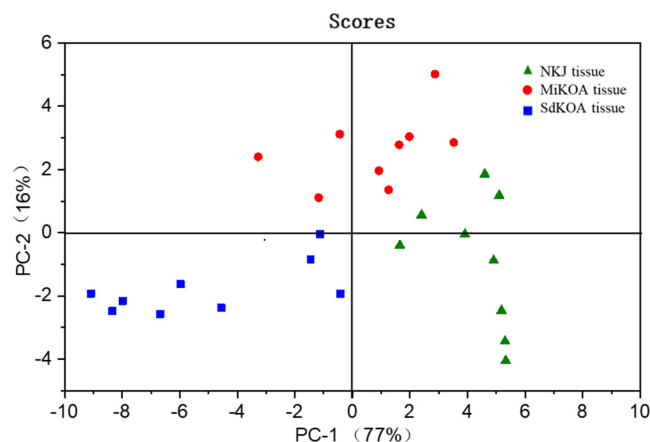

Fig. 10.   Principal component scores plot of NKJ, MiKOA and SdKOA tissues.

polysaccharide in cartilage tissue. The results are shown in Fig. 10. It can be found that NKJ samples are distributed on the right side of the scatter diagram, MiKOA samples are mainly distributed on the top of the scatter diagram, and SdKOA samples are distributed on the left side of the scatter diagram. The contribution rates of the first two principal components PC-1 and PC-2 account for 77% and 16%, respectively, accounting for 93% of the total contribution rate. This result shows that PCA based on SERS spectra in the range of 925–1025 cm^{-1} can also distinguish NKJ, MiKOA and SdKOA well, which is consistent with the result in Fig. 9, however, its resolution is slightly worse than that of Fig. 9.

4.   Conclusion

In this paper, the differences of optical properties of knee arthritis tissue and NKJ tissue were studied by using OCT and SERS technology, hoping to provide a feasible method for the early detection and diagnosis of knee arthritis. OCT images can clearly show the characteristic differences between NKJ and knee arthritis, and a series of obvious changes appear on the cartilage surface. SERS was used to study and analyze the Raman spectrum differences between NKJ and knee arthritis, and to compare the Raman characteristic peaks of MiKOA, SdKOA and NKJ tissues, which can provide judgment basis for the early detection and diagnosis of knee arthritis by analyzing the difference of tissue composition. The results show that compared with NKJ tissue, the SERS spectra signal of MiKOA and SdKOA tissue is enhanced, and the positions of the Raman peaks also change. It shows that the contents of protein, lipid and carbohydrate in the tissue have changed significantly during the course of knee joint disease. The combination of OCT, SERS spectroscopy and PCA can provide an effective reference basis for the clinical early diagnosis of knee arthritis from the aspects of morphology, optics and tissue composition. It is expected to become a new medical detection technology. Of course, at present, we can only say that in terms of theory and research results, with the deepening and development of research work, the OCT/SERS technology used in this research work may be used in clinical applications in related aspects in the future. However, at present, it is only in the research stage of *in vitro* experiment. There are still a lot of research works and technical preparations to be further improved in order to transform this method into clinical workflow and really use it in clinical application. The application of SERS is mainly used as a supplement to the application of OCT imaging. It is hoped that SERS data can provide further judgment criteria for the distinction between normal tissues and diseased tissues, and improve the reliability and accuracy of diagnosis and recognition. The sensitivity, cost and workflow of OCT/SERS mode need to be further studied in the future to obtain the experimental basis.

Conflict of Interest

Authors have no any potential conflicts of interest (professional and/or financial).

Acknowledgments

References

1. M. H. Majeed, S. A. A. Sherazi, D. Bacon, Z. H. Bajwa, "Pharmacological treatment of pain in osteoarthritis: A descriptive review," *Curr. Rheumatol. Rep.* **20**, 88 (2018).

2. C. Tu, J. He, B. Wu, W. Wang, Z. Li, "An extensive review regarding the adipokines in the pathogenesis and progression of osteoarthritis," *Cytokine* **113**, 1–12 (2019).

3. J. Gruenwald, E. Petzold, R. Busch, H. P. Petzold, H. J. Graubaum, "Effect of glucosamine sulfate with or without omega-3 fatty acids in patients with osteoarthritis," *Adv. Ther.* **26**, 858–871 (2009).

4. M. J. Lespasio, N. S. Piuzzi, M. E. Husni, G. F. Muschler, A. Guarino, M. A. Mont, "Knee osteoarthritis: A primer," *Perm. J.* **21**, 16–183 (2017).

5. E. Losina, A. M. Weinstein, W. M. Reichmann, S. A. Burbine, D. H. Solomon, M. E. Daigle, B. N. Rome, S. P. Chen, D. J. Hunter, L. G. Suter, "Lifetime risk and age at diagnosis of symptomatic knee osteoarthritis in the US," *Arthritis. Care. Res.* **65**, 703–711 (2013).

6. E. L. Kuyinu, G. Narayanan, L. S. Nair, C. T. Laurencin, "Animal models of osteoarthritis: Classification, update, and measurement of outcomes," *J. Orthop. Surg. Res.* **11**, 19 (2016).

7. S. Glyn-Jones, A. J. Palmer, R. Agricola, A. J. Price, T. L. Vincent, H. Weinans, A. J. Carr, "Osteoarthritis," *Lancet* **386**, 376–387 (2015).

8. M. B. Goldring, S. R. Goldring, "Articular cartilage and subchondral bone in the pathogenesis of osteoarthritis," *Ann. N. Y. Acad. Sci.* **1192**, 230–237 (2010).

9. T. C. Pollard, S. E. Gwilym, A. J. Carr, "The assessment of early osteoarthritis," *J. Bone Joint Surg. Br.* **90**, 411–421 (2008).

10. J. Dequeker, F. P. Luyten, "The history of osteoarthritis-osteoarthrosis," *Ann. Rheum. Dis.* **67**, 5–10 (2008).

11. C. Ding, G. Jones, A. E. Wluka, F. Cicuttini, "What can we learn about osteoarthritis by studying a healthy person against a person with early onset of disease?" *Curr. Opin. Rheumatol.* **22**, 520–527 (2010).

12. E. D. Figueiredo, G. C. Figueiredo, R. T. Dantas, "Influence of weather on osteoarthritis of the hands," *Curr. Orthop. Pract.* **24**, 171–178 (2013).

13. S. P. Messier, S. L. Mihalko, C. Legault, G. D. Miller, B. J. Nicklas, P. DeVita, D. P. Beavers, D. J. Hunter, M. F. Lyles, F. Eckstein, J. D. Williamson, J. J. Carr, A. Guermazi, R. F. Loeser, "Effects of intensive diet and exercise on knee joint loads, inflammation, and clinical outcomes among overweight and obese adults with knee osteoarthritis: The IDEA randomized clinical trial," *JAMA* **310**, 1263–1273 (2013).

14. K. Pihl, M. Englund, L. S. Lohmander, U. Jørgensen, N. Nissen, J. Schjerning, J. B. Thorlund, "Signs of knee osteoarthritis common in 620 patients undergoing arthroscopic surgery for meniscal tear," *Acta Orthop.* **88**, 90–95 (2017).

15. J. Yin, Y. Xia, "Proteoglycan concentrations in healthy and diseased articular cartilage by Fourier transform infrared imaging and principal component regression," *Spectrochim. Acta. A. Mol. Biomol. Spectrosc.* **133**, 825–830 (2014).

16. I. Afara, I. Prasadam, R. Crawford, Y. Xiao, A. Oloyede, "Non-destructive evaluation of articular cartilage defects using near-infrared (NIR) spectroscopy in osteoarthritic rat models and its direct relation to Mankin score," *Osteoarthr. Cartil.* **20**, 1367–1373 (2012).

17. R. Rudys, G. Kirdaitė, S. Bagdonas, L. Leonavičienė, R. Bradūnaitė, G. Streckytė, R. "Rotomskis, Spectroscopic assessment of endogenous porphyrins in a rheumatoid arthritis rabbit model after the application of ALA and ALA-Me," *J. PhotochemPhotobiol B* **119**, 15–21 (2013).

18. Y. Takahashi, N. Sugano, W. Zhu, T. Nishii, T. Sakai, M. Takao, G. Pezzotti, "Wear degradation of long-term *in vivo* exposed alumina-on-alumina hip joints: Linking nanometer-scale phenomena to macroscopic joint design," *J. Mater. Sci. Mater. Med.* **23**, 591–603 (2012).

19. A. Bonifacio, C. Beleites, F. Vittur, E. Marsich, S. Semeraro, S. Paoletti, V. Sergo, "Chemical imaging of articular cartilage sections with Raman mapping, employing uni- and multi-variate methods for data analysis," *Analyst.* **135**, 3193–3204 (2010).

20. R. K. Wang, V. V. Tuchin, "Optical Coherence Tomography: Light Scattering and Imaging Enhancement," Handbook of Coherent-Domain Optical Methods, pp. 665–742 (2012).

21. S. Huang, M. Shen, D. Zhu, Q. Chen, C. Shi, Z. Chen, F. Lu, "*In vivo* imaging of retinal hemodynamics with OCT angiography and Doppler OCT," *Biomed. Opt. Exp.* **7**, 663–676 (2016).

22. X. Li, S. Martin, C. Pitris, R. Ghanta, D. L. Stamper, M. Harman, J. G. Fujimoto, M. E. Brezinski, "High-resolution optical coherence tomographic imaging of osteoarthritic cartilage during open knee surgery," *Arthritis Res. Ther.* **7**, R318–R323 (2005).

23. C. W. Han, C. R. Chu, N. Adachi, A. Usas, F. H. Fu, J. Huard, Y. Pan, "Analysis of rabbit articular cartilage repair after chondrocyte implantation using optical coherence tomography," *Osteoarthr. Cartil.* **11**, 111–121 (2003).

24. C. R. Chu, D. Lin, J. L. Geisler, C. T. Chu, F. H. Fu, Y. Pan, "Arthroscopic microscopy of articular cartilage using optical coherence tomography," *Am. J. Sports Med.* **32**, 699–709 (2004).

25. T. Xie, S. Guo, J. Zhang, Z. Chen, G. M. Peavy, "Use of polarization-sensitive optical coherence tomography to determine the directional polarization sensitivity of articular cartilage and meniscus," *J. Biomed. Opt.* **11**, 064001 (2006).

26. C. R. Chu, N. J. Izzo, J. J. Irrgang, M. Ferretti, R. K. Studer, "Clinical diagnosis of potentially treatable early articular cartilage degeneration using optical coherence tomography," *J. Biomed. Opt.* **12**, 051703 (2007).

27. C. R. Chu, A. Williams, D. Tolliver, C. K. Kwoh, J. J. Irrgang, "Clinical optical coherence tomography of early articular cartilage degeneration in patients with degenerative meniscal tears," *Arthritis Rheumatol.* **62**, 1412–1420 (2010).

28. D. M. Bear, M. Szczodry, S. Kramer, C. H. Coyle, P. Smolinski, C. R. Chu, "Optical coherence tomography detection of subclinical traumatic cartilage injury," *J. Orthop. Trauma.* **24**, 577–582 (2010).

29. H. Q. Zhong, Z. Y. Guo, H. J. Wei, C. C. Zeng, H. L. Xiong, Y. H. He, S. H. Liu, "Quantification of glycerol diffusion in human normal and cancer breast tissues *in vitro* with optical coherence tomography," *Laser Phys. Lett.* **7**, 315–320 (2010).

30. H. Dong, Z. Guo, C. Zeng, H. Zhong, Y. He, R. K. Wang, S. Liu, "Quantitative analysis on tongue inspection in traditional Chinese medicine using optical coherence tomography," *J. Biomed. Opt.* **13**, 011004 (2008).

31. P. C. Lee, D. Meisel, "Adsorption and surface-enhanced Raman of dyes on silver and God sols," *J. Phys. Chem. C* **86**, 3391–3395 (1982).

32. G. H. Gu, J. S. Suh, "Enhancement at the junction of silver nanorods," *Langmuir* **24**, 8934–8938 (2008).

33. K. V. Larin, M. S. Eledrisi, M. Motamedi, R. O. Esenaliev, "Noninvasive blood glucose monitoring with optical coherence tomography: A pilot study in human subjects," *Diabetes Care* **25**, 2263–2267 (2002).

34. M. S. Dresselhaus, A. Jorio, M. Hofmann, G. Dresselhaus, R. Saito, "Perspectives on carbon nanotubes and graphene Raman spectroscopy," *Nano Lett.* **10**, 751–758 (2010).

35. G. C. Lukey, J. Deventer, S. T. Huntington, R. L. Chowdhury, D. C. Shallcross, "Raman study on the speciation of copper cyanide complexes in highly saline solutions," *Hydrometallurgy* **53**, 233–244 (1999).

36. Y. K. Kwon, M. S. Ahn, J. S. Park, J. R. Liu, D. S. In, B. W. Min, S. W. Kim, "Discrimination of cultivation ages and cultivars of ginseng leaves using Fourier transform infrared spectroscopy combined with multivariate analysis," *J. Ginseng Res.* **38**, 52–58 (2014).

37. B. Yan, B. Li, Z. Wen, X. Luo, L. Xue, L. Li, "Label-free blood serum detection by using surface-enhanced Raman spectroscopy and support vector machine for the preoperative diagnosis of parotid gland tumors," *BMC Cancer* **15**, 650 (2015).

38. C. R. Yonzon, C. L. Haynes, X. Zhang, J. T. Walsh, R. P. Van Duyne, "A glucose biosensor based on surface-enhanced Raman scattering: Improved partition layer, temporal stability, reversibility, and resistance to serum protein interference," *Anal. Chem.* **76**, 78–85 (2004).

39. Z. Movasaghi, S. Rehman, I. U. Rehman, "Raman spectroscopy of biological tissues," *Appl. Spectrosc. Rev.* **42**, 493–541 (2007).

40. S. Sigurdsson, P. A. Philipsen, L. K. Hansen, J. Larsen, M. Gniadecka, H. C. Wulf, "Detection of skin cancer by classification of Raman spectra," *IEEE Trans. Biomed. Eng.* **51**, 1784–1793 (2004).

41. P. Vandenabeele, B. Wehling, L. Moens, H. G. M. Edwards, G. V. Hooydonk, "Analysis with micro-Raman spectroscopy of natural organic binding media and varnishes used in art," *Anal. Chim. Acta.* **407**, 261–274 (2000).

42. M. Leroy, J. F. Labbé, M. Ouellet, J. Jean, T. Lefèvre, G. Laroche, M. Auger, R. Pouliot, "A comparative study between human skin substitutes and normal human skin using Raman microspectroscopy," *Acta Biomater.* **10**, 2703–2711 (2014).

43. H. Deng, V. A. Bloomfield, J. M. Benevides, J. Thomas, "Structural basis of polyamine-DNA recognition: Spermidine and spermine interactions with genomic B-DNAs of different GC content probed by Raman spectroscopy," *Nucleic Acids Res.* **28**, 3379–3385 (2000).

44. N. T. Yu, E. J. East, "Laser Raman spectroscopic studies of ocular lens and its isolated protein fractions," *J. Biol. Chem.* **250**, 2196–2202 (1975).

45. M. V. Chowdary, K. Kalyan Kumar, S. Mathew, L. Rao, C. M. Krishna, J. Kurien, "Biochemical

correlation of Raman spectra of normal, benign and malignant breast tissues: A spectral deconvolution study," *Biopolymers* **91**, 539–546 (2009).

46. Y. R. Lee, D. M. Findlay, D. Muratovic, T. K. Gill, J. S. Kuliwaba, "Raman microspectroscopy demonstrates reduced mineralization of subchondral bone marrow lesions in knee osteoarthritis patients," *Bone Rep.* **12**, 100269 (2020).